



AIAA-90-0688

**Multigrid Euler Calculations
For Three-dimensional Cascades**

F. Liu and A. Jameson

Princeton University

Princeton, NJ

28th Aerospace Sciences Meeting

January 8-11, 1990/Reno, Nevada

Multigrid Euler Calculations for Three Dimensional Cascades

Feng Liu* and Antony Jameson†
*Department of Mechanical and Aerospace Engineering
Princeton University, Princeton, NJ*

Abstract

A fast and accurate numerical method for solving the three-dimensional Euler equations is applied to cascade calculation. Test cases of a VKI turbine cascade and a low pressure turbine cascade are presented. Results of isentropic Mach number distributions on blade surfaces show good agreements with experimental data at design conditions, while discrepancy exists at off design conditions due to flow separation. With equal efficiency the method is also able to capture the basic features of secondary flow due to inlet side-wall boundary layers. Numerical results support the theory that the development of passage and horse-shoe vortices in cascades is, to a large extent, due to the inviscid convection of the inlet side-wall boundary layers.

1 Introduction

The conventional two-dimensional cascade model has been extensively used both experimentally and computationally in the development of turbomachinery blading. Requirements in the design of modern turbomachines with high efficiency and power, however, make it increasingly important that a three-dimensional model be used in the prediction of the flow in real turbomachinery blading. Three-dimensional calculations ought to be validated by a number of accurate experimental tests prior to their use in future predictions of more complex flows. While a three-dimensional Navier-Stokes solver is really needed for the above purpose, the problem of turbulence modeling and the large amount of time still necessary for Navier-Stokes solutions (for example [1]) make a fast and robust three-dimensional Euler solver a desirable tool in the design of turbomachinery blading. Beside direct application to engineering problems, solution of the Euler equations also constitutes a mid-stage in the development of reliable Navier-Stokes solvers.

In an earlier paper [2] we described the successful application of a multigrid procedure developed by the second author to calculate two-dimensional cascade flow. The present work is the three-dimensional

extension of the previous work.

The three-dimensional Euler equations are capable of capturing important three-dimensional effects due to the variation of blade sections and hub and case divergence or convergence. When proper inlet boundary conditions are given and a fine enough mesh is provided the Euler equations are also capable of capturing the major features of secondary flow vortices caused by the convection of the inlet side wall boundary layers. Although the multi-stage finite volume scheme has also been used for cascade calculations by Holmes [3] without multigrid, and by Smith and Caughey [4] with multigrid, the current work differs in many details of the method, and covers different aspects of applications. One interesting feature of this work is that the method has been applied to calculating rotational flow in an attempt to explore the possibility of predicting cascade secondary flow with an Euler code.

In the next section we will outline the basic numerical method, which uses a cell-centered finite-volume discretization coupled with a flexible multi-stage time-stepping scheme. Adaptive numerical dissipation of blended first and third differences in the same conservation form as the convection fluxes is used to provide the necessary higher order background dissipation, and the dissipation for capturing embedded shock waves. To extend the stability limit and accelerate convergence, local time stepping, enthalpy damping and residual averaging are also applied. The multigrid method which contributes much to the efficiency of our calculations will also be described. Section 3 describes the boundary conditions for typical cascade calculations. Inlet boundary conditions and the validity of enthalpy damping are discussed for the rotational flow due to end-wall boundary layers. Section 4 shows the results for two turbine cascades. Convergence histories of the numerical computations will be presented to show the efficiency of the method. Comparisons of blade isentropic Mach number distributions will be made between numerical calculation and experiment. Results of secondary flow calculations will also be presented to illustrate the capability and limitations of the inviscid calculation.

*Graduate Student, Member AIAA.

†Professor, Member AIAA.

2 Numerical Method

2.1 Finite Volume Scheme and Time Stepping

The basic numerical method is described in detail in [5, 6, 7]. Let p, ρ, u, v, w, E and H denote the pressure, density, Cartesian velocity components, total energy and total enthalpy. For a perfect gas

$$E = \frac{p}{(\gamma - 1)\rho} + \frac{1}{2}(u^2 + v^2 + w^2), \quad H = E + \frac{p}{\rho}$$

where γ is the ratio of specific heats. The Euler equations can be written in integral form as

$$\frac{\partial}{\partial t} \int_{\Omega} \mathbf{W} dV + \oint_{\partial\Omega} [\mathbf{E}dS_x + \mathbf{F}dS_y + \mathbf{G}dS_z] = 0 \quad (1)$$

for a fixed region Ω with boundary $\partial\Omega$, where

$$\mathbf{W} = \begin{bmatrix} \rho \\ \rho u \\ \rho v \\ \rho w \\ \rho E \end{bmatrix} \quad \mathbf{E} = \begin{bmatrix} \rho u \\ \rho u^2 + p \\ \rho uv \\ \rho uw \\ \rho uH \end{bmatrix}$$

$$\mathbf{F} = \begin{bmatrix} \rho v \\ \rho uv \\ \rho v^2 + p \\ \rho vw \\ \rho vH \end{bmatrix} \quad \mathbf{G} = \begin{bmatrix} \rho w \\ \rho vw \\ \rho w^2 + p \\ \rho wH \end{bmatrix}$$

The computational domain is divided into hexahedral cells (see Fig. 1). A system of ordinary differential equations can be obtained by applying equation (1) to each cell and approximating the surface integral with a finite volume scheme,

$$\frac{d}{dt}(V_{ijk} \mathbf{W}_{ijk}) + \mathbf{Q}_{ijk} = 0, \quad (2)$$

where V_{ijk} is the cell volume, \mathbf{W}_{ijk} is the average flow variable over the cell, \mathbf{Q}_{ijk} is the finite volume approximation for the net flux out of the cell. With a cell-centered scheme \mathbf{W}_{ijk} is assumed to be at the center of the cell. \mathbf{Q}_{ijk} can be evaluated as

$$\mathbf{Q}_{ijk} = \sum_{k=1}^6 [\mathbf{E}_k(\Delta S_x)_k + \mathbf{F}_k(\Delta S_y)_k + \mathbf{G}_k(\Delta S_z)_k] \quad (3)$$

Where $\mathbf{E}_k, \mathbf{F}_k$ and \mathbf{G}_k denote values of the flux vectors \mathbf{E}, \mathbf{F} and \mathbf{G} on the k -th face of the cell, $(\Delta S_x)_k, (\Delta S_y)_k$ and $(\Delta S_z)_k$ are the x, y, z components of the face area vector. $\mathbf{E}_k, \mathbf{F}_k$ and \mathbf{G}_k can be evaluated by taking the averages of \mathbf{E}, \mathbf{F} and \mathbf{G} respectively on either side of the cell face.

The scheme constructed in this manner reduces to a central difference scheme on Cartesian meshes, and is second order accurate if the mesh is sufficiently smooth. However a central difference scheme

will permit modes with odd and even decoupling. To prevent this and to capture shocks without pre-shock oscillations, an additional dissipation term is added to the semi-discrete equation (2) so that we solve

$$\frac{d}{dt}(V_{ijk} \mathbf{W}_{ijk}) + \mathbf{Q}_{ijk} - \mathbf{D}_{ijk} = 0, \quad (4)$$

where

$$\mathbf{D}_{ijk} = (D_x + D_y + D_z) \mathbf{W}_{ijk}$$

and

$$D_x \mathbf{W}_{ijk} = \mathbf{d}_{i+\frac{1}{2},j,k} - \mathbf{d}_{i-\frac{1}{2},j,k}$$

The dissipation fluxes $\mathbf{d}_{i+\frac{1}{2},j,k}$ are defined as a blending of first and third differences

$$\mathbf{d}_{i+\frac{1}{2},j,k} = \epsilon_{i+\frac{1}{2},j,k}^{(2)} R_{i+\frac{1}{2},j,k} \Delta_x \mathbf{W}_{i,j,k} + \epsilon_{i-\frac{1}{2},j,k}^{(4)} R_{i+\frac{1}{2},j,k} \Delta_x^3 \mathbf{W}_{i-1,j,k} \quad (5)$$

where Δ_x is the forward difference operator defined by

$$\Delta_x \mathbf{W}_{ijk} = \mathbf{W}_{i+1,j,k} - \mathbf{W}_{ijk}$$

$R_{i+\frac{1}{2},j,k}$ is a coefficient chosen to give the dissipative terms the proper scale. It is usually taken to be the spectral radius of the Jacobian matrix of $(\mathbf{E}\Delta S_x + \mathbf{F}\Delta S_y + \mathbf{G}\Delta S_z)$, where $\Delta S = (\Delta S_x, \Delta S_y, \Delta S_z)$ is the face area vector in the i direction. It must be pointed out that the above differences are formed of ρH rather than ρE for the energy equation. The purpose of this is to allow a steady state solution for which H remains constant.

The second term on the right hand side of Eqn. (5) is of third order compared to the surface flux terms in Eqn. (3). It is used to eliminate the odd and even decoupling and does not destroy the second order accuracy of the scheme. The first term in Eqn. (5), however, consists of the first difference of \mathbf{W}_{ijk} . It is introduced to provide the necessary first order dissipation for capturing shocks. To preserve second order accuracy in regions away from shocks we define a shock sensor

$$\nu_{ijk} = \left| \frac{p_{i+1,j,k} - 2p_{i,j,k} + p_{i-1,j,k}}{p_{i+1,j,k} + 2p_{i,j,k} + p_{i-1,j,k}} \right| \quad (6)$$

and let

$$\epsilon_{i+\frac{1}{2},j,k}^{(2)} = \kappa^{(2)} \max(\nu_{i+1,j,k}, \nu_{i,j,k})$$

Here the parameter $\kappa^{(2)}$ is $O(1)$. It has been found necessary to switch off the third differences near shocks and this can be done by letting

$$\epsilon_{i+\frac{1}{2},j,k}^{(4)} = \max(0, \kappa^{(4)} - \epsilon_{i+\frac{1}{2},j,k}^{(2)})$$

Exactly similar terms can be constructed for $D_y \mathbf{W}_{ijk}$ and $D_z \mathbf{W}_{ijk}$. Thus in smooth regions of flow, the quantity in Eqn. (6) is of second order

so that the dissipative terms are still of third order. When the pressure undergoes a rapid change, ν_{ijk} and thus $\epsilon_{i+\frac{1}{2},j,k}^{(2)}$ are $O(1)$. The dissipation is then of first order in the presence of rapid changes in pressure but of third order wherever the flow variations are smooth.

Equation (4) is integrated in time by an explicit multistage scheme. Since the cell volume V_{ijk} is independent of time Eqn. (4) can be written as

$$\frac{d\mathbf{W}_{ijk}}{dt} + \mathbf{R}_{ijk}(\mathbf{W}) = 0 \quad , \quad (7)$$

where \mathbf{R}_{ijk} is the residual

$$\mathbf{R}_{ijk}(\mathbf{W}) = \frac{1}{V_{ijk}} (\mathbf{Q}_{ijk} - \mathbf{D}_{ijk}) \quad .$$

Let \mathbf{W}^n be the value of \mathbf{W}_{ijk} after n time steps. Dropping the subscripts i, j, k the general m stage hybrid scheme to advance a time step Δt can be written as

$$\begin{aligned} \mathbf{W}^{(0)} &= \mathbf{W}^n \\ \mathbf{W}^{(1)} &= \mathbf{W}^{(0)} - \alpha_1 \Delta t \mathbf{R}^{(0)} \\ &\dots \\ \mathbf{W}^{(m-1)} &= \mathbf{W}^{(0)} - \alpha_{m-1} \Delta t \mathbf{R}^{(m-2)} \\ \mathbf{W}^{(m)} &= \mathbf{W}^{(0)} - \Delta t \mathbf{R}^{(m-1)} \\ \mathbf{W}^{n+1} &= \mathbf{W}^{(m)} \end{aligned}$$

where the residual at each stage is evaluated as a linear combination of the flux and dissipation terms at current and previous stages subject to a consistency requirement (see [5]).

Multistage schemes are chosen because of their extended stability limit and high frequency damping properties which are appropriate for multigrid schemes. For our calculations we have used a 5 stage scheme with evaluations of the dissipation term only at the first, third and fifth stages. The coefficients are chosen to be

$$\alpha_1 = 1/4, \quad \alpha_2 = 1/6, \quad \alpha_3 = 3/8, \quad \alpha_4 = 1/2 \quad .$$

Detailed analysis of the properties of the scheme can be found in [5]. The allowable Courant number for the 5 stage scheme is 4.0. This number can still be increased by smoothing the residuals at each stage. This is done in the following product form in three-dimensions.

$$(1 - \epsilon_x \delta_x^2)(1 - \epsilon_y \delta_y^2)(1 - \epsilon_z \delta_z^2) \bar{\mathbf{R}}_{ijk} = \mathbf{R}_{ijk}$$

Where ϵ_x, ϵ_y and ϵ_z are the smoothing parameters in each direction. Since it is only necessary to solve a sequence of tridiagonal equations for separate scalar variables, this scheme has the advantage over other implicit schemes that it requires a relatively small amount of computational effort per time step.

It can be shown for a one-dimensional model problem without dissipation that the scheme can be

made stable for any Courant number provided the smoothing parameter is large enough [5]. In our calculation best convergence is achieved at Courant numbers around 9 with minimum smoothing. In order to further increase the rate of convergence, locally varying time steps and enthalpy damping can also be used. Both of these techniques are based on the assumption that the solution approaches a steady state, and thus will not work for time accurate solutions.

2.2 Multigrid Method

The most effective method of accelerating convergence, however, is the multigrid method. Auxiliary meshes are introduced by doubling the mesh spacing and values of the flow variables are transferred to a coarser grid by the rule

$$\mathbf{W}_{2h}^{(0)} = \sum V_h \mathbf{W}_h / V_{2h}$$

where the subscripts denote values of the mesh spacing parameter. In three dimensions the sum is over the 8 cells on the fine grid composing each cell on the coarse grid. The rule conserves mass, momentum and energy. A forcing term is then defined as

$$\mathbf{P}_{2h} = \sum \mathbf{R}_h(\mathbf{W}_h) - \mathbf{R}_{2h}(\mathbf{W}_{2h}^{(0)})$$

where \mathbf{R} is the residual of the difference scheme. To update the solution on a coarse grid the multistage scheme is reformulated as

$$\begin{aligned} \mathbf{W}^{(1)} &= \mathbf{W}_{2h}^{(0)} - \alpha_1 \Delta t (\mathbf{R}_{2h}^{(0)} + \mathbf{P}_{2h}) \\ &\dots \\ \mathbf{W}^{(q+1)} &= \mathbf{W}_{2h}^{(0)} - \alpha_q \Delta t (\mathbf{R}_{2h}^{(q)} + \mathbf{P}_{2h}) \\ &\dots \end{aligned} \quad (8)$$

where $\mathbf{R}^{(q)}$ is the residual of the q -th stage. In the first stage of the scheme, the addition of \mathbf{P}_{2h} cancels $\mathbf{R}_{2h}(\mathbf{W}^{(0)})$ and replaces it by $\sum \mathbf{R}_h(\mathbf{W}_h)$, with the result that the evolution on the coarse grid is driven by the residual on the fine grid. This process is repeated on successively coarser grids. Finally the correction calculated on each grid is passed back to the next finer grid by bilinear interpolation. In the present implementation a W -cycle strategy is used in each time step.

Since the evolution on a coarse grid is driven by residuals collected from the next finer grid, the final solution on the fine grid is independent on the choice of dissipation and boundary conditions on the coarse grid when the computation converges. To reduce the computational effort we can use a simpler first difference dissipation on the coarse grid in place of the blended first and third dissipation in Eqn. (5). The same boundary conditions discussed in the next section are applied to all boundaries on all levels of grids for cascade calculations. It is important

in cascade calculations to update inlet and outlet boundary conditions in the multigrid, since solutions at these boundaries do change a lot during the course of solution. This is unlike the far field for an external flow, where the conditions can be frozen on the coarse grids to save computational time.

The success of a multigrid scheme is critically dependent on the high frequency damping property of the time stepping scheme. The 5 stage scheme seems to offer a good choice for this purpose.

3 Boundary Conditions

At present H-type meshes are used. For cascade calculations we usually encounter four types of boundaries: wall, periodic, inlet and outlet. For wall boundaries zero normal velocity is imposed, and we use the normal momentum equation to extrapolate the pressure to the wall. For periodic boundaries Equivalent flow variables are imposed at corresponding cells.

At the inlet boundary four of the five independent flow variables must be specified for subsonic inlet flow. The other flow variable must be extrapolated from inside the flow field according to characteristic analysis. In light of actual experimental conditions we choose to specify the total enthalpy, entropy, which is equivalent to total pressure, and the two independent flow angles of the incoming flow. The one-dimensional Riemann invariant normal to the flow boundary is used to obtain the other condition. Let subscript ∞ denote upstream values, and let q_n be the velocity component in the direction of the outer normal of the inlet boundary and c the speed of sound. The outgoing one-dimensional characteristic equation can be written as

$$q_n + \frac{2}{\gamma - 1} c = q_{n\infty} + \frac{2}{\gamma - 1} c_{\infty} \quad (9)$$

The conditions for the entropy, enthalpy and flow angles can be written as

$$S = S_{\infty} \quad (10)$$

$$H = H_{\infty} \quad (11)$$

$$\frac{u}{q} = \cos \beta_x, \quad \frac{v}{q} = \cos \beta_y, \quad \frac{w}{q} = \cos \beta_z \quad (12)$$

where S_{∞} , H_{∞} , β_x , β_y , and β_z are the given entropy, total enthalpy and flow angles. β_x , β_y , and β_z satisfy the following conditions

$$\cos^2 \beta_x + \cos^2 \beta_y + \cos^2 \beta_z = 1 \quad (13)$$

With the above equations we can solve for all the flow variables on the boundary, or rather with a cell centered scheme flow variables on the fictitious cells adjacent to the boundary. For supersonic inlet flow all flow variables are specified.

Conversely on the outlet boundary, only the pressure is specified for subsonic flow, while entropy, total enthalpy or the outgoing one-dimensional Riemann invariant, and flow angles are extrapolated. For outlet flow with supersonic axial velocity all variables are extrapolated.

Although in general the total enthalpy in viscous flow is not constant it is approximately constant in a boundary layer when Prandtl number of the fluid is one. Therefore it is reasonable to assume that the inlet flow is of constant total enthalpy, and thus the whole flow is of constant enthalpy for our inviscid flow calculations. Furthermore the static pressure at the inlet cross section can be assumed to be constant. In this way specifying the inlet velocity profile is equivalent to specifying an entropy profile or stagnation pressure. Also since the total enthalpy is constant, our acceleration scheme of enthalpy damping may still be applied.

One interesting phenomena in the inviscid calculation with an inlet boundary layer is that the inviscid "boundary layer" cannot sustain any adverse pressure gradient. Fig. 2 shows three cases of inviscid flow of a boundary-layer type velocity profile in a channel. Case (a) is a constant area channel which gives no pressure gradient and thus the flow maintains its original velocity profile downstream. Case (b) is a converging channel and gives a negative pressure gradient. The fluid at the wall will then expand to a lower pressure and thus have non-zero velocity at the wall downstream. Case (c) has a diverging channel and thus a positive pressure gradient. Notice that the static pressure at the entrance is just the stagnation pressure of the fluid near the wall. As the main flow goes downstream its velocity decreases. The pressure in the fluid near the wall cannot, however, be further increased in an inviscid flow, and thus the flow will be driven backwards. This property of inviscid flow can be subtly important in the treatment of boundary conditions.

In applying the boundary conditions the stagnation pressure at the inlet is calculated from the velocity profile, which is usually taken from experiment or otherwise estimated, under the condition of known enthalpy and static pressure. With a boundary layer the static pressure is just the stagnation pressure at the wall where the velocity is zero. Therefore specifying a stagnation pressure profile in fact fixes the static pressure at the inlet which, however, in the subsonic case should be determined by the exit boundary conditions, usually the back pressure. Therefore we may expect to encounter problems with over-specifying flow conditions. A slight inconsistency of inlet static pressure may occur for a given back pressure, even if the inlet stagnation pressure profile is taken from experimental data. If the solution happens to yield a lower static pressure than the stagnation pressure at the inlet, the

fluid will then expand and yield a non-zero velocity at the wall. If the solution happens to yield a higher static pressure, the flow at the inlet will then separate at the walls. Fig. 3 shows such a case as occurred in one of our calculations when we had a stagnation pressure profile calculated from a velocity profile whose static pressure corresponds to Mach number 0.4 while the real Mach number is around 0.1 for an exit isentropic Mach number of 0.7. After the flow evolves into a certain stage the flow develops two separation regions at the inlet. These regions of backward flow then cause difficulty in convergence, since the treatment of inlet boundary conditions assumes an incoming flow while the fluid is in fact going out of the boundary. Even if we can solve the convergence problem by using outgoing flow boundary condition in these regions it is still questionable if such a flow can truly exist or be uniquely determined independently of the initial flow field in our time marching solution, since the outgoing fluid comes from separation bubbles that could be isolated from the main flow.

4 Computational Results

4.1 VKI Turbine Cascade

The VKI turbine nozzle proposed for validating numerical methods [9] was used as a test case for our previous two-dimensional program[2]. We applied our present three-dimensional program to solve the same problem and the results are found to be identical to our two-dimensional solution. A 77×21 H-mesh shown in Fig. 4 with the same surface definition as proposed in [9] was used in the blade to blade plane. The interior points of the mesh are redistributed by an elliptic mesh generator after Thompson, Thames and Mastin [8]. A three-dimensional mesh is constructed by stacking 11 of these two-dimensional H-meshes in the span-wise direction, forming a three-dimensional linear cascade with straight side walls.

Fig. 5 shows the convergence history of a transonic calculation for an exit isentropic Mach number of 0.7. The computation was done with 2 levels of multigrids. Within 200 time steps, which is equivalent in work to 225 time steps of single-grid calculation if we neglect the work involved in transferring data between the fine and coarse grids, the residual, shown by the solid line in fig 5, is driven to the order of 10^{-10} . The dashed line shows the relative difference between the mass flow at the exit and that at the entrance of the cascade. With this difference driven to the order of 10^{-10} we can be sure that our calculation properly conserves mass flow in the cascade passage, which is an important property for internal flow calculations. Although we have carried out 200 time steps, the mass flow difference and

the out flow angle shown in fig. 5 indicates that the calculation has reached a steady state in a few more time steps than 50.

Fig. 6 shows the blade surface isentropic Mach number distributions of both experiment[9] and our calculation at the above exit conditions. The comparison shows good agreement except at the trailing edge of the blade. This is because we did not use any cusp to modify the round trailing edge which causes an extreme suction peak in the inviscid flow solution. We will further address the trailing edge problem in the next test case.

Fig. 7 shows the solution of the same cascade at exit isentropic Mach number 1.0. Convergence for this transonic calculation is almost equivalent to the previous subsonic case. Good agreement with experimental data is also obtained. More accurate solutions, particularly near the round trailing edge, could only be achieved by a viscous flow model or by adding an appropriate cusp. Nevertheless the fast convergence and fairly good agreement with experimental data without adding a cusp, and with just a straight forward H-mesh, shows the robustness of the scheme.

Since the Euler equations are capable of describing rotational flow one expects that they can be used to solve flow fields that involve inviscid vortex transport. In cascade problems secondary flow is not only important for the performance of turbomachines but also interesting, because there has been the suggestion that certain features of the secondary flow are due to the inviscid convection of the vortices developed on the side walls at the entrance. If this is so, the Euler equations should be able to predict these features of the secondary flow when given the initial boundary-layer type velocity distribution. The origin of this velocity distribution is of course due to viscosity. However the later development of the vortex flow and its effects on the global flow field, such as the appearance of passage vortices, may be largely an inviscid process. To demonstrate this idea we solved the Euler equations for the VKI cascade with a typical inlet boundary layer velocity distribution. For this calculation 21 grid points are used in the span-wise direction. They are distributed in such a way that the grid has a better resolution near the end-walls to capture the boundary-layer type velocity profile.

Fig. 8 shows the swirl in two cross sections of the cascade flow field. The swirl is defined to be the dot product of the vorticity and velocity vectors normalized by the magnitude of the velocity. Therefore it is essentially the streamwise vorticity and can be used as a good indication of secondary flow. Cross section A-A cuts through the two counter rotating horse shoe vortices generated in front of the leading edge as a consequence of the interaction of the side wall boundary layers and the blade. Each of the

horse shoe vortices branch into two legs downstream on either side of the blade. The branches on the pressure side, however, have the same sense of rotation as the passage vortices generated by the the pressure gradient between the upper and lower blades, and thus can not be distinguished from the larger passage vortices. The suction side branch of the horse shoe vortices have the opposite sense of rotation and can be still seen downstream in cross section B-B. Notice that in Fig. 8 the velocities in section A-A are actually toward the blade suction surface, and thus the swirl of the two vortices has just the opposite signs to that of the passage vortices in section B-B. Although quantitative comparison of the secondary flow with experiments is not available, the qualitative results seem encouraging. In the next section we present some comparisons with experiments for a carefully measured turbine cascade.

4.2 Denton's Test Case E/CA-7

This test case is recommended by Denton[10]. It is a cascade of turbine blades with profile typical of the root section of a low pressure aircraft gas turbine. Its side walls have a 6° divergence in the blade passage. The cascade has been extensively tested and analyzed by Hodson and Dominy at the Whittle Lab, Cambridge, England[11, 12, 13].

At its design condition this cascade has an exit isentropic Mach number of 0.7 and an incidence angle of 38.8 degrees. We calculated this case with a $80 \times 16 \times 16$ mesh. Fig. 9 is the typical convergence history for our calculations with 3 levels of multigrid. Fig. 10 shows the isentropic Mach number distribution at mid-span together with the experimental data taken from [12]. It is pointed out in [12] that there is a separation bubble at about 0.8 chord on the upper surface of the blade. This seems to explain the slight discrepancy between the experimental data and our inviscid solution. The inviscid solution gives a greater adverse pressure gradient than the real viscous flow. The viscous flow cannot sustain the large adverse pressure and thus separates, changing the outer inviscid flow.

Notice that our solution also predicts a suction peak near the leading edge. This can also be seen in the pressure contour plot in Fig. 11. This suction peak is followed by a sharp diffusion, and therefore is likely to cause separation too. Although the experimental data do not show this suction peak, Hodson[11] observed a small separation bubble near the leading edge. In fact at a larger incidence angle this suction peak becomes obvious in the measured data too. Fig. 12 shows the computed and measured isentropic Mach number distribution at an 8 degree positive incidence angle off design condition. The measured data is taken from [13]. We can see that the leading-edge suction peak on the upper surface

is increased while that on the lower surface disappears. Overall agreement between experiment and computation is still obtained.

Fig. 13 shows another off-design condition with a 20 degree negative incidence angle. We see that in this case there is a large discrepancy between calculation and experiment on the lower blade surface. At 20 degree's negative incidence angle, there is a long separation bubble on the lower surface after the leading edge as observed by Hodson[13]. The extreme diffusion in that region predicted by the inviscid solution is in fact a good signal of the existence of separation. There is also a discrepancy between our computation and experiment on the upper surface. It is likely, however, that the large separation bubble on the lower surface affects the solution on the upper surface too.

It must be pointed out that for this cascade we have purposely sharpened the trailing edge of the blade to avoid the suction spike as found in the previous VKI case. This also improves the entropy contamination in the region due to the inaccuracy of the scheme in resolving a high gradient 'inviscid' flow around blunt round corners. Inviscid solutions are not unique for a rounded trailing edge if a Kutta condition is not explicitly imposed. With an Euler solver the position of the tip of the trailing edge is important in determining the Kutta condition. One has to be very careful as to how to place a cusp at the trailing edge. We find that a well chosen rigid cusp for the design condition may not be good at all for off design conditions. In fact it may lead to a rather erroneous load on the blade, implying that the Kutta condition is not properly satisfied. In light of this we have only removed the trailing edge circle to yield a sharpened edge instead of adding an extended cusp. This seems to give the right overall load on the blade even though the details at the trailing edge do not compare as well with experimental data. For an accurate resolution of the flow at the trailing edge and a unique determination of the solution at all conditions a viscous model must be used. If an Euler method is to be used for more careful studies of cascade flow one may use a non-rigid or even a "transparent" cusp that allows for mass flux, to simulate the trailing edge. One criterion for such a cusp is that the cusp should not carry any load [3, 14].

To simulate secondary flow in this cascade we can use the end wall velocity profile measured by Hodson to obtain the entropy profile at the entrance. In terms of isentropic Mach number distribution at mid-span there is in fact not much difference between the solution of uniform inlet flow and that of a boundary-layer inlet flow. This difference, of course, becomes significant near the end walls. Fig. 14 is the spanwise variation of pitchwise mixed-out flow angle. We can see a great overturning of the flow near

the end-walls due to the low speed in the "boundary layer". This overturning is then followed by an underturning some distance into the flow field. This is due to the velocity induced by the horse-shoe vortex convected down stream from the leading edge. Notice that the underturning can not be adequately captured if a coarse mesh is used. Fig. 15 shows that the peak value of this underturning agrees well with Hodson's experimental data on a $160 \times 32 \times 64$ mesh. 64 cell volumes are used in the spanwise direction since this cascade has a large aspect ratio and there is also the boundary layer near the end walls. Even on this fine mesh with an inlet boundary layer the convergence rate remains fast. The average residual is reduced to the order of 10^{-11} after 100 time steps with 4 levels of multigrid. It can be seen, however, that the position of our peak is displaced toward the end-walls. This shift of peak position may be at least partly explained by the fact that a real viscous boundary layer grows in thickness while our fictitious inviscid one does not. The growth of the real boundary layer will displace the fluid away from the wall and thus cause the vortex to be further pushed inside.

Fig. 15 shows the secondary velocity vector field and vortex contours at 140% Cx. The secondary velocities were obtained by projecting the velocity vectors onto the plane perpendicular to the mixed-out flow direction at the section. The vorticity is then calculated on that plane and plotted with plot3d. Comparison with that obtained by Hodson (Fig. 16) from experiment shows that although the positions of the vortices do not agree very well with experiments our computational results predict essentially the same vortex structure.

5 Concluding remarks

A finite volume method with a multi-stage time stepping scheme is used to calculate three-dimensional cascade flow with end wall boundary layer type velocity profiles. The stability limit of the explicit scheme is extended by using implicit residual averaging. Convergence is accelerated by using local time stepping, enthalpy damping and most of all a multigrid method. The method has been applied to the VKI turbine nozzle, and a low pressure turbine cascade with end wall boundary layer profiles. Convergence is achieved generally within 50-100 time steps. The algorithm of the method is systematic and very well vectorizable. A calculation of 50 time steps on a $77 \times 21 \times 11$ mesh takes 208 seconds on a Convex C-210 vector machine including IO time. Comparisons with experiments show a fairly good accuracy of our method for an Euler solver. Calculations were done without adding a cusp to the usually round trailing edge of turbine blades. Com-

putational results also verify the idea that the Euler equations are capable of capturing the secondary flow vortices which develop as a consequence of inviscid convection of the entrance velocity profile. Work is currently under way to extend the method to treat the Navier-Stokes equations with a turbulence model.

References

- [1] Dawes W. N. "Development of a 3D Navier Stokes Solver for Application to all types of Turbomachinery", ASME paper 88-GT-70, 1988
- [2] Jameson, A., and Liu, F., "Multigrid calculations for Cascades", in *Lecture Notes in Physics*, Dwoyer D. L. and Hussaini M. Y. and Voigt R. G. eds., Springer-Verlag, 1989
- [3] Holmes, D. G. and Tong, S. S. "A Three-Dimensional Euler Solver for Turbomachinery Blade Rows", *J. of Engineering for Gas Turbines and Power*, Vol. 107, April 1985
- [4] Smith, W. A. and Caughey, D. A. "Multigrid Solution of Inviscid Transonic Flow through Rotating Blade Passages", AIAA Paper 87-0608
- [5] Jameson, A., *Transonic Flow Calculations*, MAE Report #1651, Princeton University, July 1983
- [6] Jameson, A., and Baker, T. J., "Solution of the Euler Equations for Complex Configurations", AIAA Paper 83-1929, 1983
- [7] Jameson, A., and Baker, T. J., "Multigrid Solution of the Euler Equations for Aircraft Configurations", AIAA Paper 84-0093, 1984
- [8] Thompson, J. F., Thames, F. C. and Mastin, C. W., "Automatic Numerical Generation of Body-Fitted Curvilinear Coordinate Systems for Fields Containing Any Number of Arbitrary Two-dimensional Bodies", *Journal of Computational Physics*, 15, 299-319(1977)
- [9] Sieverding C. "Test Case 1: 2-D Transonic Turbine Nozzle Blade", in *Numerical Methods for Flows in Turbomachinery Blading*, VKI lecture Series 1982-05, April 26-30, 1982
- [10] Denton J. D. "Test Case Number E/CA-7, The La Turbine Cascade", Private Communication, April, 1989
- [11] Hodson H. P. and Dominy R. G., "Boundary Layer Transition and Separation Observed near the leading Edge of a High Speed Turbine

Blade", ASME J. Eng. for G.T. & Power, Vol 107, Jan. 1985

- [12] Hodson H. P. and Dominy R. G., "Three-Dimensional Flow in a Low Pressure Turbine Cascade at its Design Condition", ASME paper 86-GT-106, 1986
- [13] Hodson H. P. and Dominy R. G., "The Off-Design Performance of a Low Pressure Turbine Cascade", ASME paper 86-GT-188, 1986
- [14] He, L., Whittle Laboratory, Cambridge University, Cambridge, UK. *Private Communications*, 1989

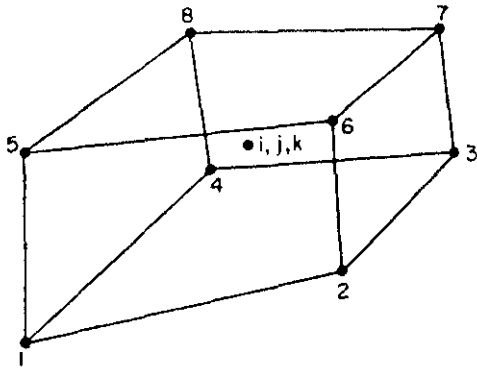


Fig. 1. Hexahedral Cell Around Point (i, j, k)

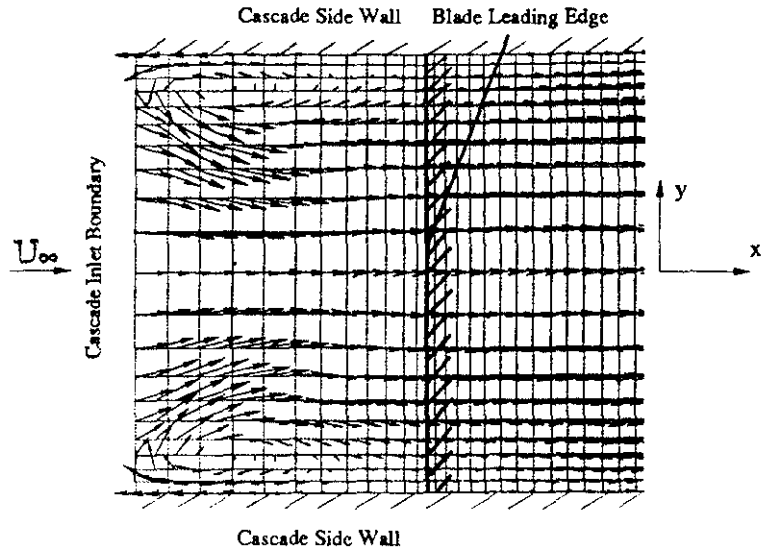


Fig. 3. Velocity Vectors on a Blade to Blade Surface Through the VKI Cascade

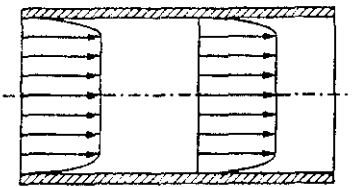


Fig. 2(a) Inviscid Flow in a Constant Area Channel with a Boundary Layer Velocity Profile

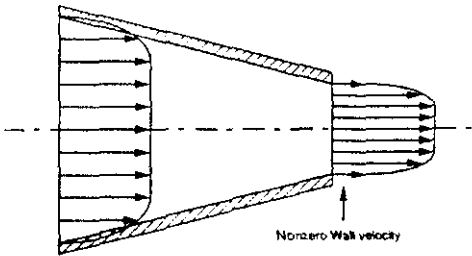


Fig. 2(b) Inviscid Flow in a Converging Channel with a Boundary Layer Velocity Profile

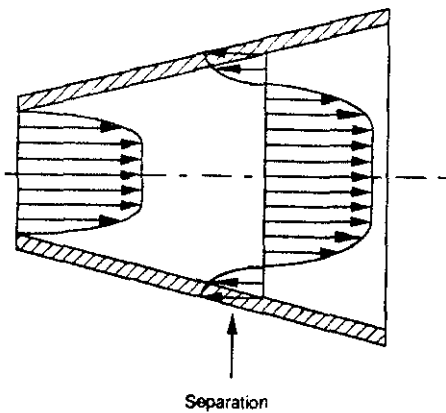


Fig. 2(c) Inviscid Flow in a Diverging Channel with a Boundary Layer Velocity Profile

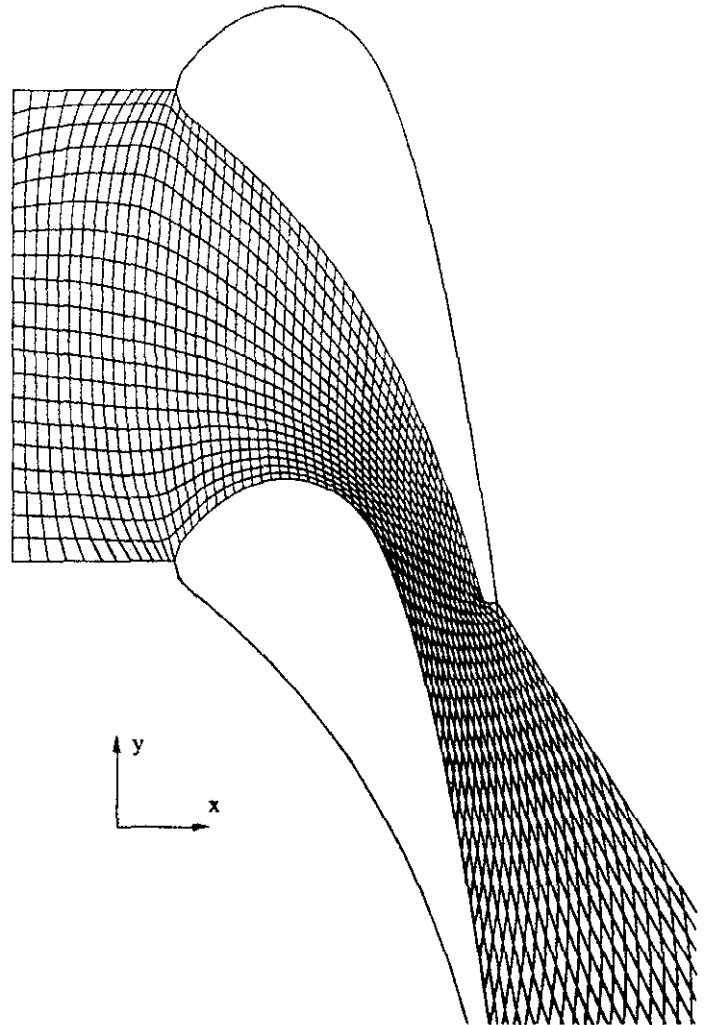
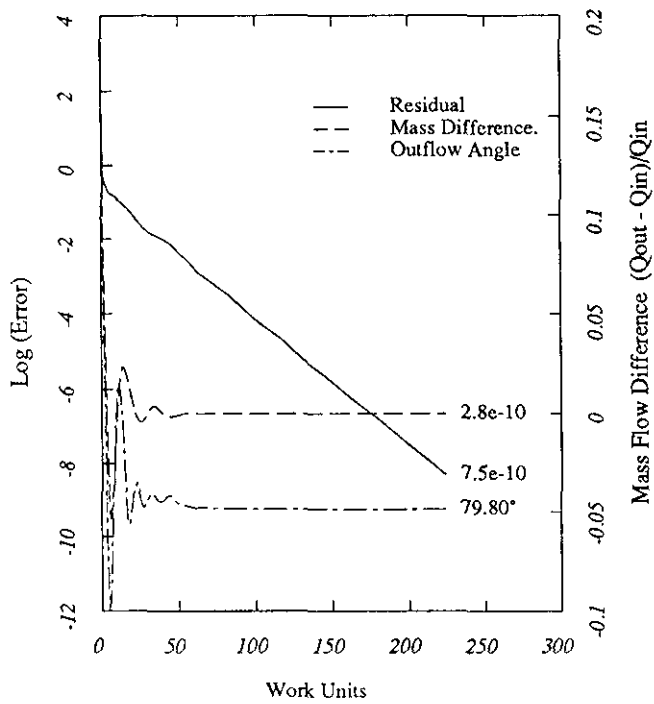


Fig. 4. Geometry and Grid Lines of the VKI Cascade



Ncyc: 200 Resid1: 0.1500 Resid2: 7.5e-10
Rate1: 0.9182 Rate2: 0.9084
76x20x10 mesh, 2 level(s) of multigrid W-Cycle

Fig. 5. Convergence History for the VKI Cascade

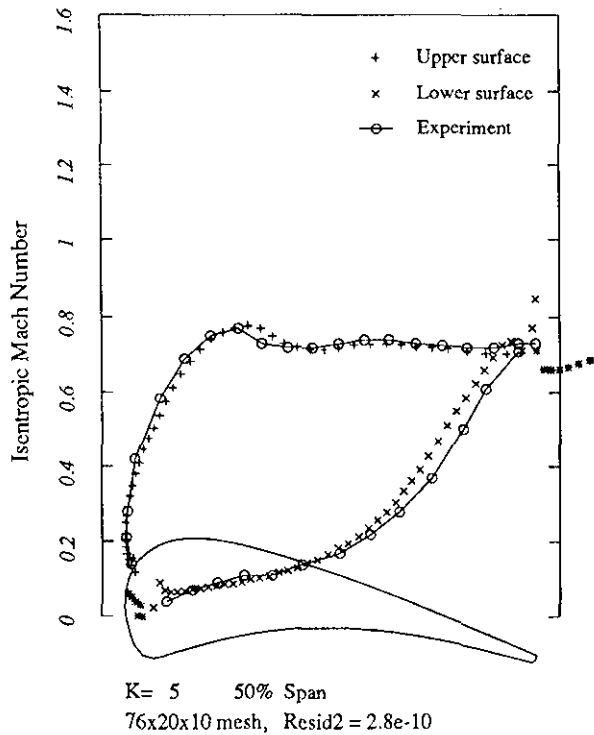


Fig. 6. Isentropic Mach Number Distribution over the VKI Cascade at Exit Isentropic Mach Number 0.7

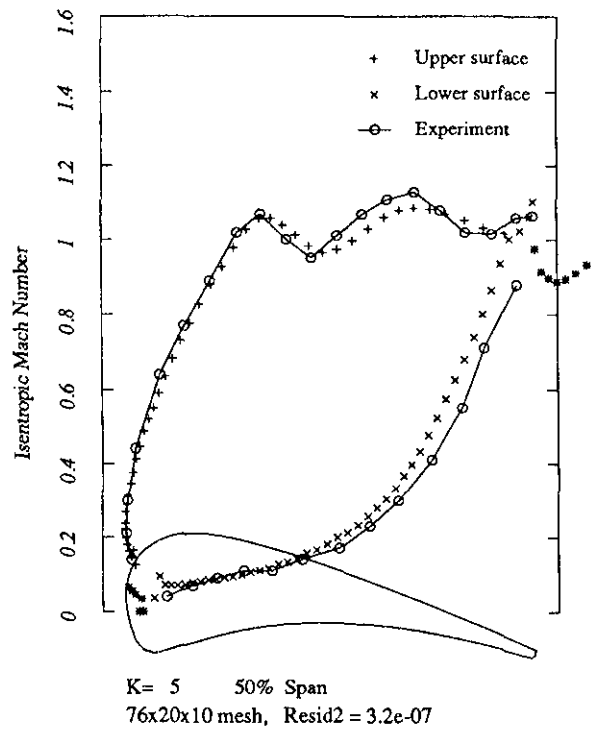


Fig. 7. Isentropic Mach Number Distribution over the VKI cascade at Exit Isentropic Mach Number 1.0

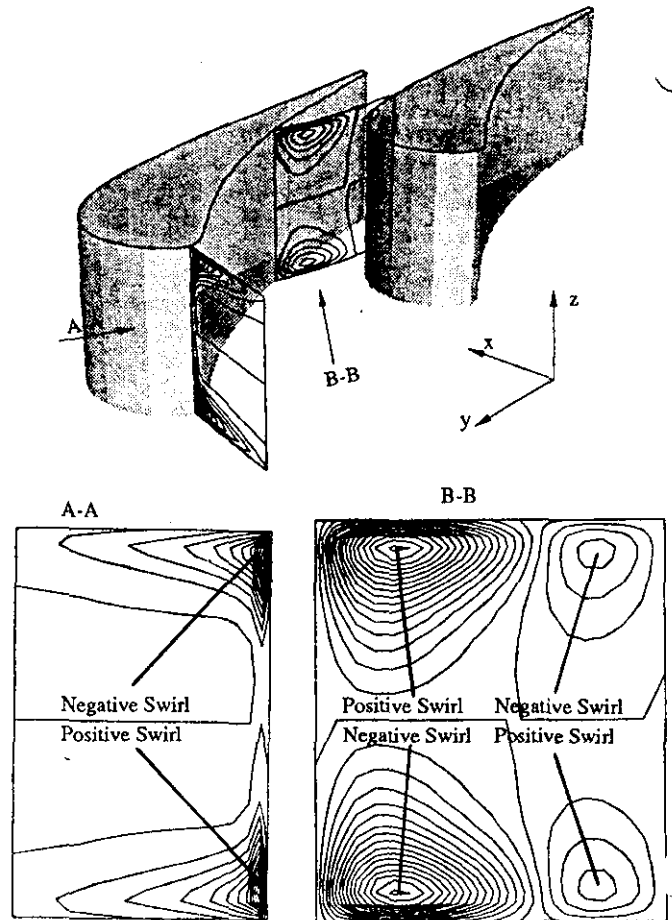


Fig. 8. Swirl Contours of the VKI Cascade on two Cross Section Planes

Fig. 10. Isentropic Mach Number Distribution over the E/CA-7 cascade at Exit Isentropic Mach Number 0.7

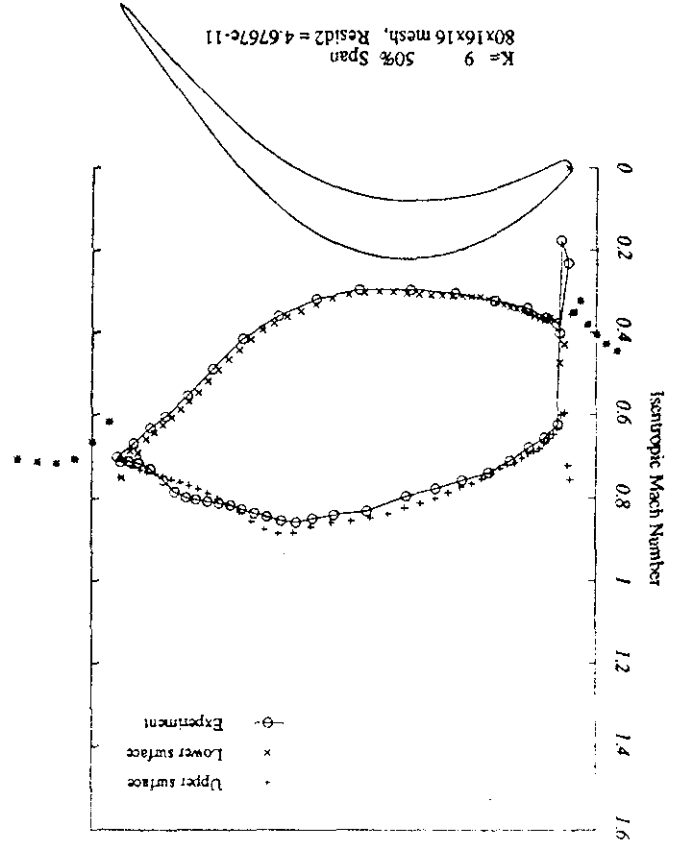


Fig. 9. Convergence History for the E/CA-7 Cascade

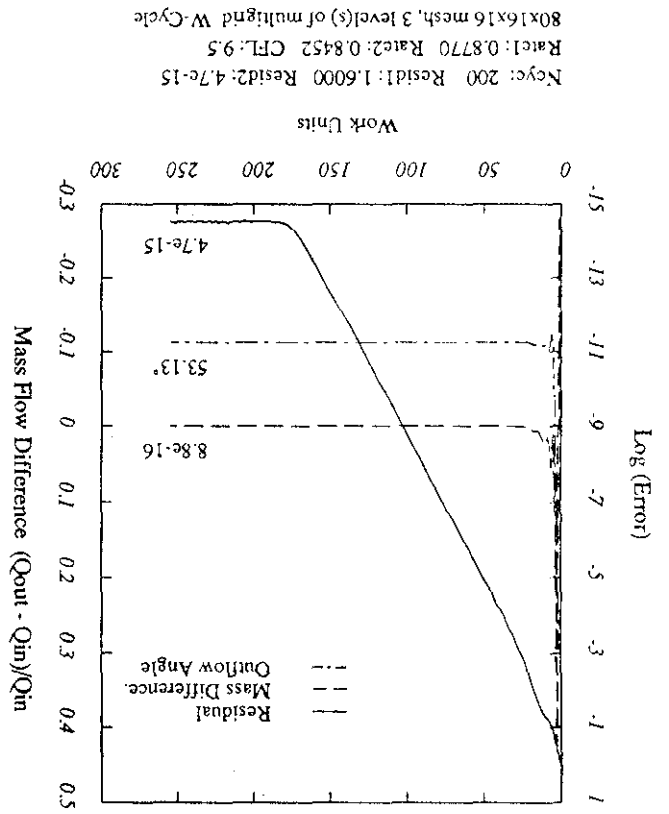


Fig. 12. Isentropic Mach Number Distribution over the E/CA-7 Cascade at 8° Incidence Angle

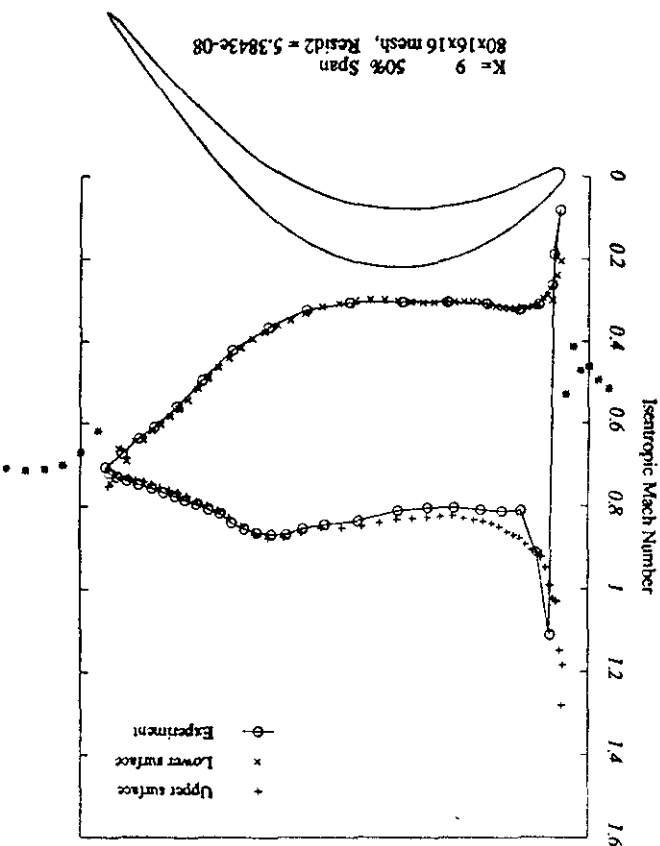
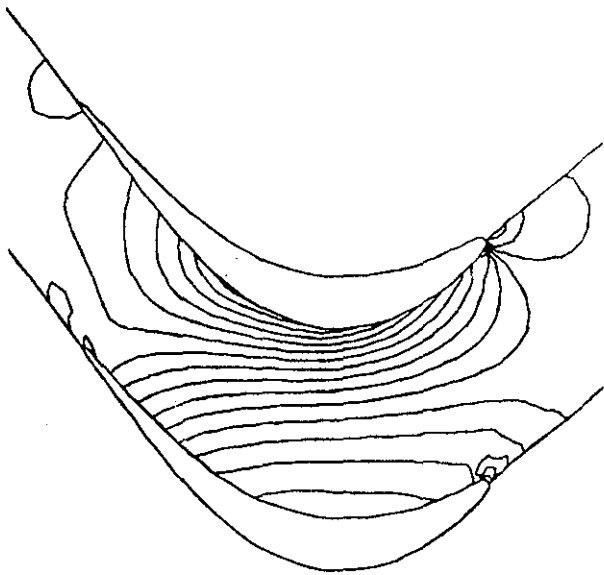


Fig. 11. Pressure Contours of the E/CA-7 Cascade



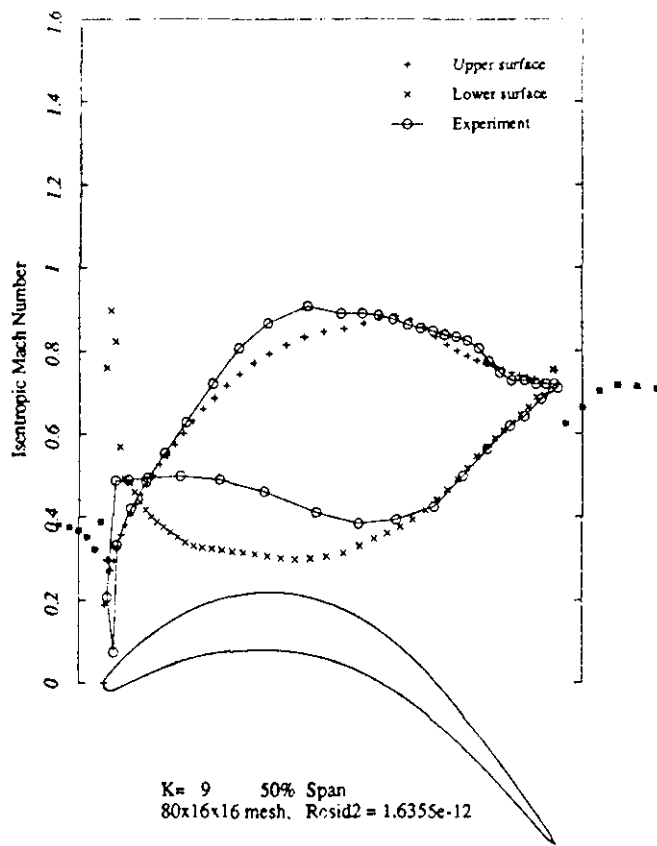


Fig. 13. Isentropic Mach Number Distribution over the E/CA-7 Cascade at -20° Incidence Angle

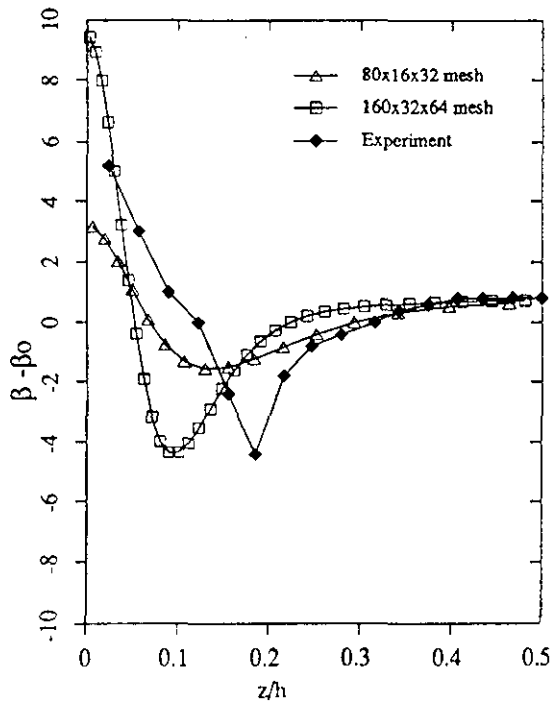


Fig. 14 Pitchwise-mixed Exit Flow Angle Distribution

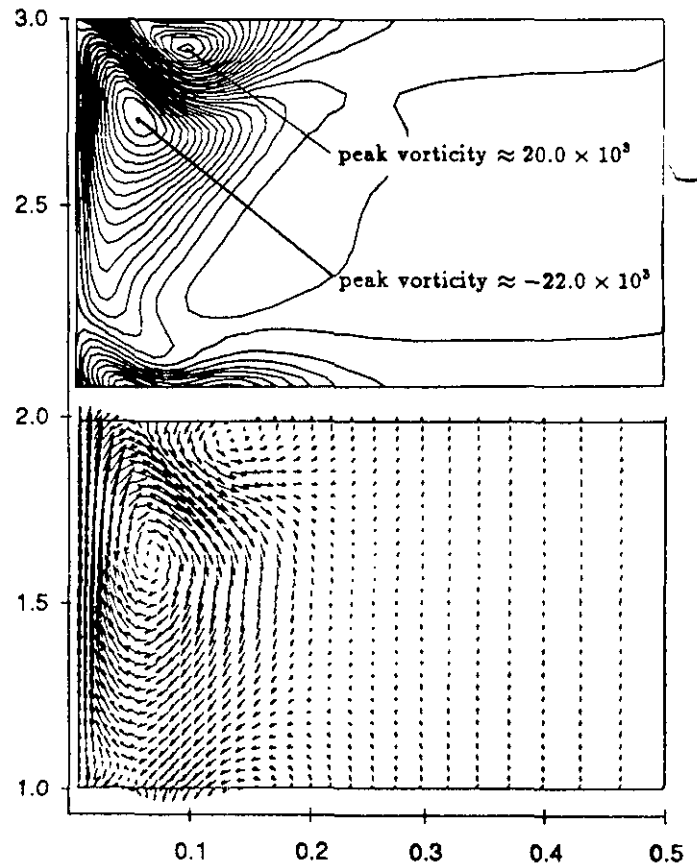


Fig. 15. Secondary Velocity Vectors and Vorticity Contour at $x/C_x = 140\%$

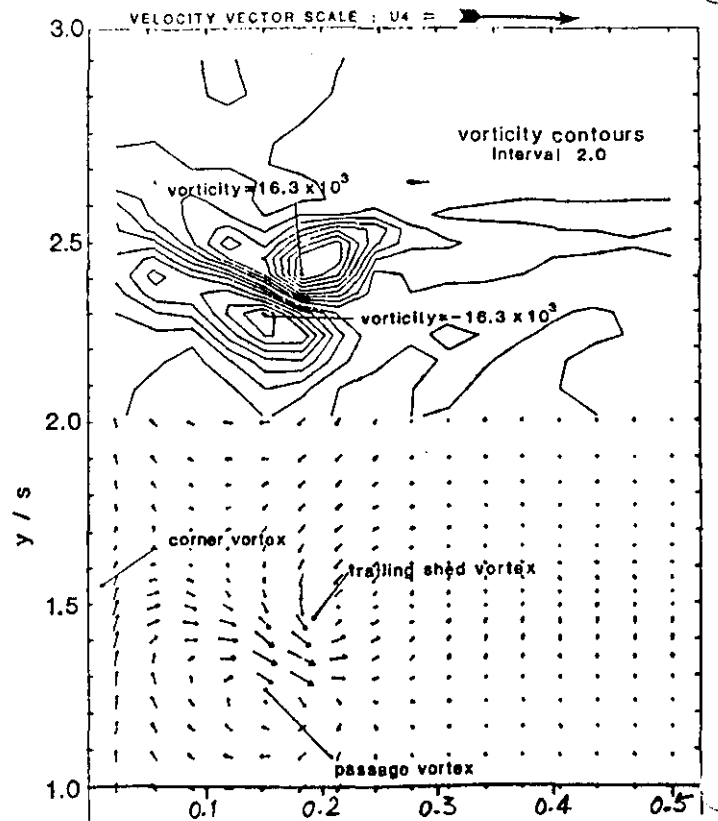


Fig. 16. Experimental Secondary Velocity Vectors and Vorticity Contour at $x/C_x = 140\%$ [12]